ACS OMEGA

http://pubs.acs.org/journal/acsodf

Article

Water-Immersion Laser-Scanning Annealing for Improving Polycrystalline Au Films

Shang-Yang Yu, Min-Hsiung Shih, Yun-Cheng Ku, Yi-Han Kuo, and Jiunn-Woei Liaw*

Cite This: *ACS Omega* 2022, 7, 42272−42282

Read Online

ACCESS | Metrics & More | Article Recommendations | Supporting Information

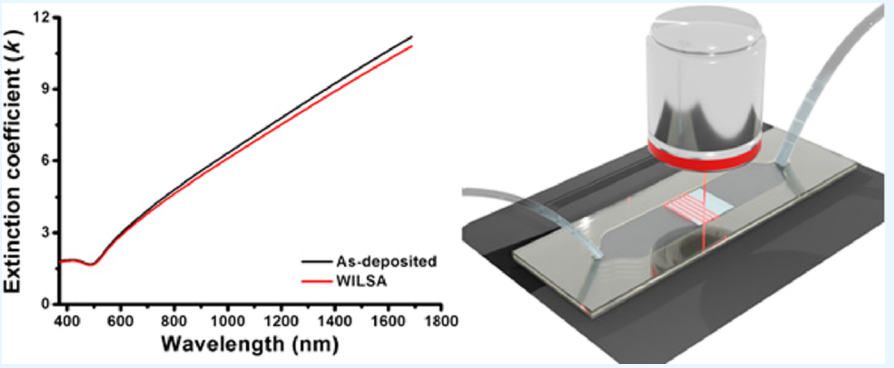

ABSTRACT: A water-immersion laser-scanning annealing (WILSA) method was developed for the heat treatment of a deposited polycrystalline Au film on a glass. The material characterization using X-ray diffraction, field-emission scanning electron microscopy, and electron backscatter diffraction shows improved crystallinity with a more uniform crystallographic orientation of (111) and the grain growth of the annealed Au film. Additionally, the optical constants of the Au film before and after annealing were characterized by spectroscopic ellipsometry in the visible to near-infrared (NIR) regime, and the corresponding optical densities (ODs) were measured by transmittance spectroscopy. Our results show that the extinction coefficient and the OD of the annealed film are significantly reduced, particularly in the NIR regime. This is because the grain growth caused by the annealing reduces the density of grain boundaries, leading to the decrease of the loss of free electrons' scattering at grain boundaries. Hence, the damping effect of the surface plasmon is reduced. Additionally, the integrity of the WILSA-treated thin film is kept intact without pinholes, usually produced by the conventional thermal annealing. Based on the improved optical property of the WILSA-treated Au film, two performances of an insulator−metal−insulator (IMI) layered structure of biosensors are theoretically analyzed. Numerical results show that the propagation length of a long-range surface plasmon polariton along an IMI structure with an annealed Au film is significantly increased, compared to an unannealed film, particular in the NIR region. For the other application of using an IMI sensor to detect the shift of the surface-plasmon-resonance dip in the total internal reflection spectrum for the measurement of a change of the medium's refractive index, the sensitivity is also profoundly improved by the WILSA method. It is worth mentioning that the optimal heating conditions (laser wavelength, fluence, exposure time, and scanning step) depend on the thickness of the Au film. Our study provides a postprocess of WILSA to improve the optical properties of a deposited polycrystalline Au film for raising the sensitivity of the related biosensors.

INTRODUCTION

Physical vapor deposition (PVD), for example, thermal or electron-beam evaporation, is commonly used to produce a deposited metal thin film, such as Cu, Au, Ag, or Al. The optoelectronic properties of these polycrystalline films produced by PVD are critical to the substrate temperature, the deposition rate, and the pressure in the deposition chamber.[1,2] To improve the optoelectronic properties of these films, a postprocess of thermal annealing or rapid thermal annealing is usually required to induce grain growth and improve crystallinity.[3−9] In addition, the material modification facilitates the fabrication of nanostructures on the metal film via focused ion beam (FIB) milling.[10] Because of the grain growth induced by the annealing, the density of grain boundaries is reduced to diminish the loss of free electrons' scattering from the grain boundaries. This modification is particularly useful for reducing the loss of surface plasmon resonance (SPR) of metallic nanostructures. The SPR behavior

Received: August 9, 2022
Accepted: October 20, 2022
Published: November 7, 2022

is a strong collection motion of free electrons in metal, driven by the incident light in a specific frequency regime of ultraviolet to near-infrared (NIR). The mean free path of free electrons in Au is about 37.7 nm.[11] This implied that as the area fraction of the grains of a size less than 40 nm increases, the scattering effect of free electrons interacting with grain boundaries becomes severe. Consequently, the damping of the SPR effect, an interaction of photons with free electrons, is more severe.

Spectroscopic ellipsometry was usually used to characterize the optical properties of a metal thin film.[12−22] For this measurement, the data of the multiple incidence angles are required for cross-checking.[18] The accuracy of the measure of dielectric constants (permittivity) is usually related to the thickness of the metal film and the adhesion layer. In addition, the Kramers−Kronig (K−K) model is used for the curve-fitting of optical constants or dielectric constants of the metal film, a lossy material, to obey a constraint of the linear causality for the dielectric constants of metal.[18,19] In addition, several material characterization methods were usually used to measure the grain size and the orientation of (111), such as field-emission scanning electron microscopy (FE-SEM), electron backscatter diffraction (EBSD), X-ray diffraction (XRD), and atomic force microscopy.[23−25]

Because of the SPR effect, a variety of plasmonic sensors have been developed in the past decades.[25−34] Several important applications of Au thin films for various biosensors are based on a typical configuration of the insulator−metal−insulator (IMI) layered structure. For example, the long-range surface plasmon polariton (LRSPP) along an IMI layered structure is commonly applied for the waveguides or biosensors, particularly in the NIR regime.[4] Another application of an IMI sensor is for the measurement of the change of the medium's refractive index by detecting the shift of the SPR dip in the total internal reflection spectrum.[24−26] In general, a postprocess of annealing for a deposited Au film can improve the sensitivity of these SPR sensors.[24−26] However, several types of defects induced by the thermal annealing are usually observed, such as the bulges (blisters), solid state dewetting, and pinholes (voids).[35−40] These induced defects are also related to the quality of the adhesion layer, the delamination of film, the local overheating, and Rayleigh instability.[34−40] The preservation of the film integrity after the annealing is essential for the following fabrication of nanostructures via FIB milling.

Recently, laser-scanning annealing methods have been proposed and developed for the annealing of metal films in air or vacuum.[22,41−46] Because of the SPR effect of metal, the photothermal heating on the metal film is enhanced. The advantage of laser-scanning annealing is to provide a temperature gradient in the metal film for the migration of grain boundaries; this could facilitate the grain growth locally. According to the simulations of the Monte-Carlo Potts model, the grain boundary migrations depend on the temperature gradient in the heat-affected zone.[47−49] Using a 2D laser-scanning path, the entire area of a metal film can be covered. Although the local laser heating can improve the grain growth, the local laser heating in air or vacuum is very difficult to control.[44] The overheating could cause the local deformation or even melting. As a result, the morphology of nanostructures could be changed, which is not preferred.[44]

On the other hand, previous research studies have shown that the optical performance of a single-crystalline waveguide is superior to that of a polycrystalline plasmonic waveguide or sensor.[50] A variety of approaches for fabricating single-crystalline metal films were developed, such as the chemically synthesized single-crystalline microflakes,[51−53] the molecule beam epitaxy method,[54−59] and the chemical wet method (e.g., epitaxial electrochemical deposition).[60−64] However, from the practical aspect there are certain limitations in applying these single-crystalline methods in the fabrication of a realistic plasmonic device.

In this paper, we study the performance of a water-immersion laser-scanning annealing (WILSA) method developed for the heat treatment of a polycrystalline Au film deposited on a glass. This postprocess is conducted in a fluidic chamber with a room-temperature water supply. The purpose of this annealing design is to promote the local grain growth and to improve the crystallinity of the Au film mildly. An advantage of this method is that the local overheating is avoided by utilizing the high heat capacity of water to carry away the excess heat in the Au film. Hence, the solid-state dewetting and Rayleigh instability can be prevented; the former is related to the adhesion layer. Typically, the melting point of a nanostructure is much lower than that of the bulk material. For example, the melting point of bulk gold is about 1064 °C, whereas that of the Au thin film could be as lower as 520 °C, depending on the thickness. We conjecture that the temperature range of gold's Rayleigh instability is about 420−500 °C. Additionally, because of the low heat capacity of gold and the high thermal conductivity, it is challenging to control the temperature inside the Au thin film during the laser heating. Of interest is that the temperature inside the Au film might be above 350 °C during the laser heating, whereas the temperature outside the film is above room temperature a little without causing the boiling of water. Although the mechanism is unclear, the nanoscale thermal conduction at the interface between Au and water could play an important role.[65] Another advantage of the point-scanning laser heating is to provide a temperature gradient in the Au film to facilitate the migration of grain boundaries. Consequently, the integrity of the WILSA-treated thin film could be preserved intact without producing pinholes, which are easily caused by the thermal annealing. After the WILSA treatment, the material properties are characterized by XRD, FE-SEM, and EBSD. According to the suggestion of previous research studies,[2,66] the optical constants as well as the optical density (OD) of the Au film will also be measured to investigate whether the optical property of the WILSA-treated Au film is improved or not; the former is measured by the variable-angle spectroscopic ellipsometry and the latter by the transmission spectrometer. In particular, the reduction of the extinction coefficient of the Au film in the NIR regime, which is a crucial indication, will be verified. Additionally, the integrity of the annealed film will be examined. Moreover, the optical constants of the unannealed and the annealed Au films will be used to analyze the performances of two applications of IMI structures for comparison. Additionally, the optical constants of Johnson and Christy (J&D) will be compared with ours.[67]

METHOD

Sample Preparation. The polycrystalline Au films were deposited on a glass (1 mm × 1 mm × 0.3 mm) by an electron-beam evaporator (PEVA-900, AST) with a deposition rate of 1−3 Å/s. The nominal thickness of the Au film is 150 nm. Because the adhesion between the Au film and the glass

https://doi.org/10.1021/acsomega.2c05101
ACS Omega 2022, 7, 42272−42282

substrate is not good, an adhesion layer of Ti with a thickness of 5 nm between them was used to ensure the adhesion quality of the multilayered structure, particularly during the annealing.

WILSA System. The schematic of the setup of the WILSA system, the water chamber, and the scanning path are shown in Figure 1a. A fiber-couple compact laser source (LuxX diode

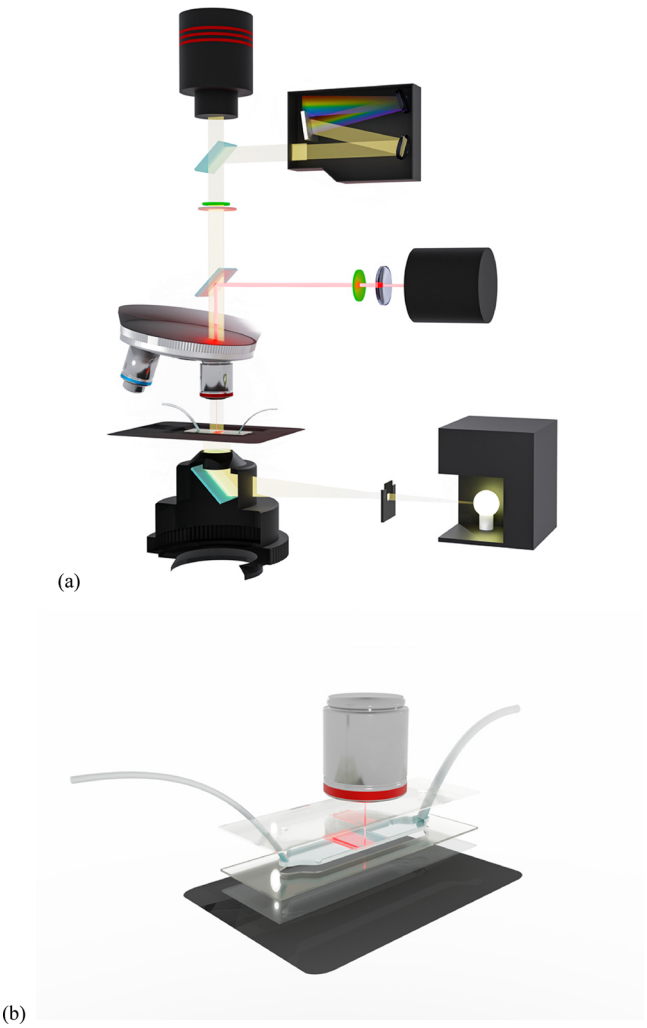

Figure 1. (a) Schematic of a WILSA system with a CW laser, installed in a microscope. (b) Configuration of a specimen treated by a laser beam in a fluidic chamber. The laser-scanning path is multiline zigzag.

lasers series hub with 515, 638, and 830 nm; Omicron Laser, Germany) was mounted at the upper stand of an upright microscope (Axio Imager Z2, Carl Zeiss Co. Ltd., Germany) with motorized $x-y$ stages (Scanning Stage 130 × 85 STEP(D) for Axio Imager, Physik Instrumente, Germany). The laser beam through the upper stand is reflected by a dichroic beam-splitter (FF721-SDi01-25 × 36, Semrock, USA) and then is focused into a specimen in a water cooling channel by an objective lens (5×, NA: 0.16). Figure 1b shows the configuration of a specimen treated by a laser beam in a fluidic chamber. The isometric laser-scanning path is the multiline zigzag. The pitch between adjacent laser spots along a line is Δx, and the pitch between adjacent lines is Δy. For a CW laser of λ = 830 nm through an objective lens (5×, NA: 0.16), the focal spot size is about 6 μm. The output power of the laser beam through the objective lens (5×) is 50 mW, tunable by a software package (Omicron Laser). The scanning path interlocked with motorized $x-y$ stages is controlled by a software package (Zen Blue, Carl Zeiss Co. Ltd., Germany) for setting the displacement, the speed/acceleration of the stage movement, and the dwelling time of point-scanning. The scanning step is Δx = 30 μm for x-axis and Δy = 20 μm for y-axis, and the scanning duration is 0.5 s/position. Two $\lambda/4$ plates are inserted in the upper stand and the lower stand to control the polarization of laser and the white light source, respectively. Because of the plasmonic photothermal effect, a polycrystalline Au film is annealed at a high temperature for the grain growth. The uniqueness of this method is that the temperature inside the Au film could be 300−400 °C, whereas the surrounding water temperature for cooling is slightly above room temperature. The specimen is placed inside a water channel, made of polydimethylsiloxane (PDMS), on a glass slide hold by a mounting frame of the motorized $x-y$ stages properly. The water flow rate is controlled by a peristaltic pump.

The advantage of the point-scanning laser heating is to generate a temperature gradient in the heat-affected zone, which facilitates a local grain growth and drives the migration of grain boundaries. In principle, the optimal annealing temperature at the laser-spot area in the Au film is between 300 and 400 °C for the grain growth. Above 420 °C, the local Rayleigh instability could be easily induced, a transition state of partial solid and liquid phases as the temperature is near the melting point. When the Rayleigh instability occurs, the surface tension of the liquid portion could reshape the morphology of the nanostructure.[43] Therefore, we use room-temperature water, instead of air, as the surrounding medium to provide a high-heat-capacity thermal reservoir, which can regulate the heating to avoid a local solid-state dewetting or Rayleigh instability in the Au film.[35,36] This mild annealing process can promote the local grain growth and avoid the local Rayleigh instability. In addition, the bulges (blisters), solid-state dewetting, or pinholes (voids) in a deposited thin film during annealing, usually produced in conventional thermal annealing, must be avoided. Notice that these defects are also related to the condition of the adhesion layer. The laser heat-treated area is 5 mm × 5 mm. After the WILSA process, the optical quality and the integrity of the treated Au film are assessed by this microscopy. A halogen lamp is the light source for the bright-field image and the OD measurement. The magnification of the objective lens is 40× (NA: 0.65).

Material Characterization. The grain size, size distribution, and uniformity of the Au film's crystalline structure were analyzed by EBSD (Nordlys Max3, Oxford Instruments, Abingdon, UK) equipped with a FE-SEM (JSM-7800F PRIME, JEOL, Tokyo, Japan), operated at 20 kV. The surface morphology images were captured at 10 kV by another FE-SEM (JSM-7610F, JEOL, Tokyo, Japan). The grain-size distribution of EBSD was analyzed by a software package (OIM Analysis, EDAX of AMETEK Inc., PA, USA). Additionally, the crystallinity was measured by XRD at a sampling interval of 0.01° (D8 ADVANCE ECO, BRUKER, MA, USA) to quantize the variations of crystal orientations.

Optical Characterization. The optical constants of Au films before and after laser annealing were measured by spectroscopy ellipsometry (M-2000, J.A. Woollam Co., NE, USA). We used an embedded function of K−K mode in the CompleteEASE software (J.A. Woollam Co., NE, USA) for the curve-fitting of the dielectric constants of Au to maintain the

https://doi.org/10.1021/acsomega.2c05101
ACS Omega 2022, 7, 42272−42282

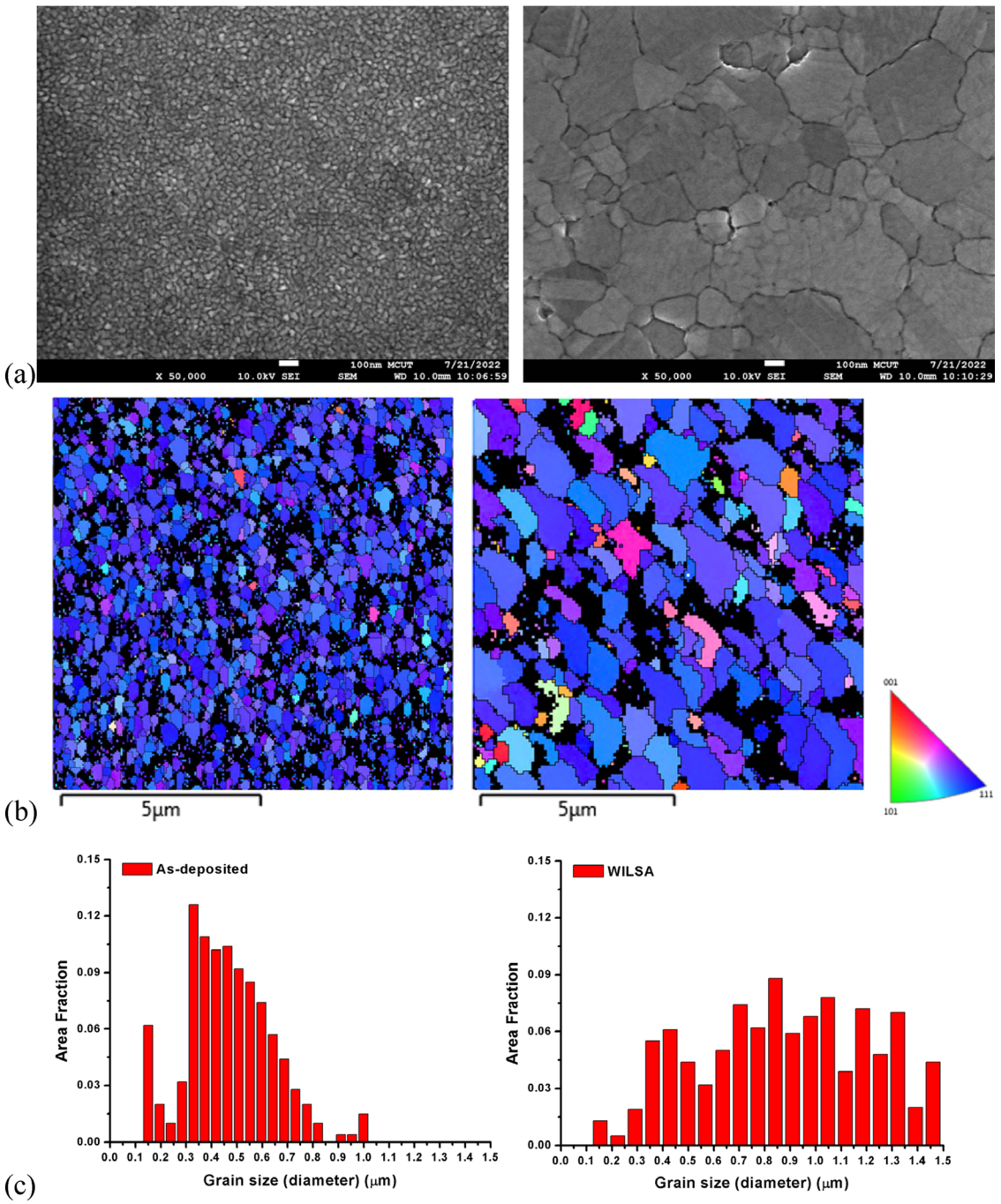

Figure 2. (a) FE-SEM images (acceleration voltage: 10 kV) of the unannealed and the WILSA-treated Au films (JSM-7610FPlus, Schottky field-emission scanning electron microscope, cold field, WD: 10 mm). (b) EBSD orientation maps in *Z*-direction (acceleration voltage: 20 kV; JSM-7800F PRIME and Nordlys Max3, JEOL, Japan) and inverse pole figure. The black areas are the amorphous or the nanograin with a size less than 50 nm. The crystallographic orientation of the grains (111) is dominant. (c) Grain-size distributions of both cases. Left: Unannealed Au film. Right: WILSA-treated Au film.

consistency of the linear causality in the whole spectrum physically. The data of the multiangle (45°, 55°, 65°, and 75°) measurements were analyzed. In addition, the transmission spectra of the Au film before and after laser annealing were measured using a spectrometer (QE-pro, Ocean Insight, FL, USA) in the microscope, as shown in Figure 1a. From the transmission spectrum, the OD of the Au film can be obtained. In particular, the integrity of the annealed Au film can also be assessed by the bright-field image acquired by the CCD of this microscope. The light source for the OD measurement and the bright-field image is a halogen lamp.

RESULTS AND DISCUSSION

First, several specimens of 150 nm Au films deposited on a glass with a 5 nm Ti adhesion layer were prepared. Subsequently, they were processed by the WILSA method. The annealing laser power is 50 mW, and the dwell time at each spot is 0.5 s. For the point-scanning along a zigzag path, the pitch between adjacent spots along the x-axis is Δx = 30

https://doi.org/10.1021/acsomega.2c05101
ACS Omega 2022, 7, 42272−42282

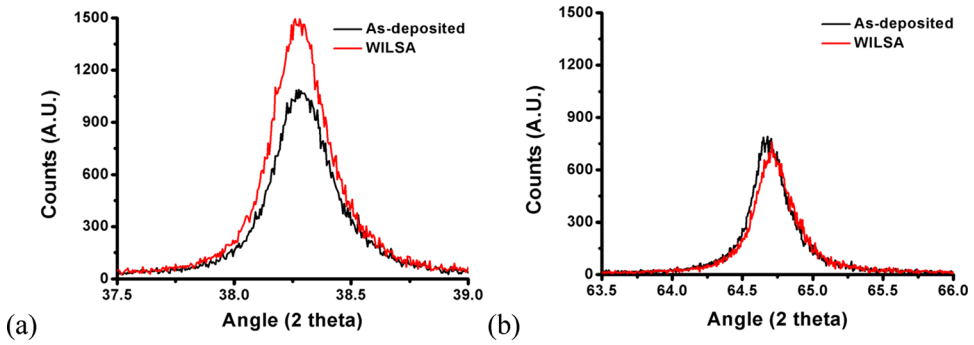

Figure 3. Intensities of XRD of the Au film before and after WILSA treatment at the orientations of (a) (111) and (b) (220). The former is at 38.2° and the latter at 64.7°.

μm, and the distance between adjacent lines is Δy = 20 μm. In addition, the material and optical characterization studies of these Au films before and after annealing were performed to evaluate and compare their performances.

Material Characterization. Figure 2a,b shows the grain images of FE-SEM and EBSD of Au films before and after the WILSA treatment. The grain-size distributions are shown in Figure 2c. The resolution of EBSD for measuring the grain size is about 100 nm. The results show that the WILSA treatment significantly induces the grain growth in the Au film. The EBSD orientation maps indicate that (111) is the primary orientation. Obviously, the area fraction of the micron-sized grain is increased a lot by the WILSA treatment, in comparison of the distributions in Figure 2c. Based on this finding, we can infer that the energy loss of free electrons colliding the grain boundaries is reduced, which will be exhibited in the following optical measurement of the extinction coefficient. The density of the grain boundary is reduced to decrease the plasmonic damping because of the collision of electrons with the grain boundary. Figure 3 shows the intensities of XRD at the (111) and (220) orientations; the former is at 38.2° and the latter at 64.7°. Again, the results illustrate that the WILSA treatment significantly improves the crystal orientation of (111) of the Au film. In contrast, the WILSA treatment does not affect the (220) orientation.

In addition, the WILSA method can keep the integrity of the Au film without inducing pinholes or the other defects, which are usually produced by a conventional thermal annealing in a furnace (Figure S1 in the Supporting Information). The mechanism of the induced defects (voids or pinholes) by the conventional thermal annealing could be due to a competitive growth of multiple grains at the same time caused by a uniform temperature field. In general, the compactness of a deposited film by the PVD method is not perfect, depending on the deposition rate and the substrate temperature. As multiple grains grow simultaneously and their crystallinity increases during the thermal annealing, these internal tiny nanovoids inside the film would be driven to aggregate at the grain boundaries. Consequently, larger voids or pinholes are formed during the conventional thermal annealing. Figure 4 shows the pinholes in the Au film induced by the conventional thermal annealing at 400 °C for 1 h in a furnace (SJ-OV400, Lindberg/Blue M, USA); a typical size of pinholes is 353 nm. From the FE-SEM image of Figure 4b, the grain growth of the Au film, caused by the thermal annealing, is observed. In contrast, the WILSA method provides a point-scanning heating to cause a local grain growth, where the induced temperature gradient field allows the migration of the grain boundaries. As a result,

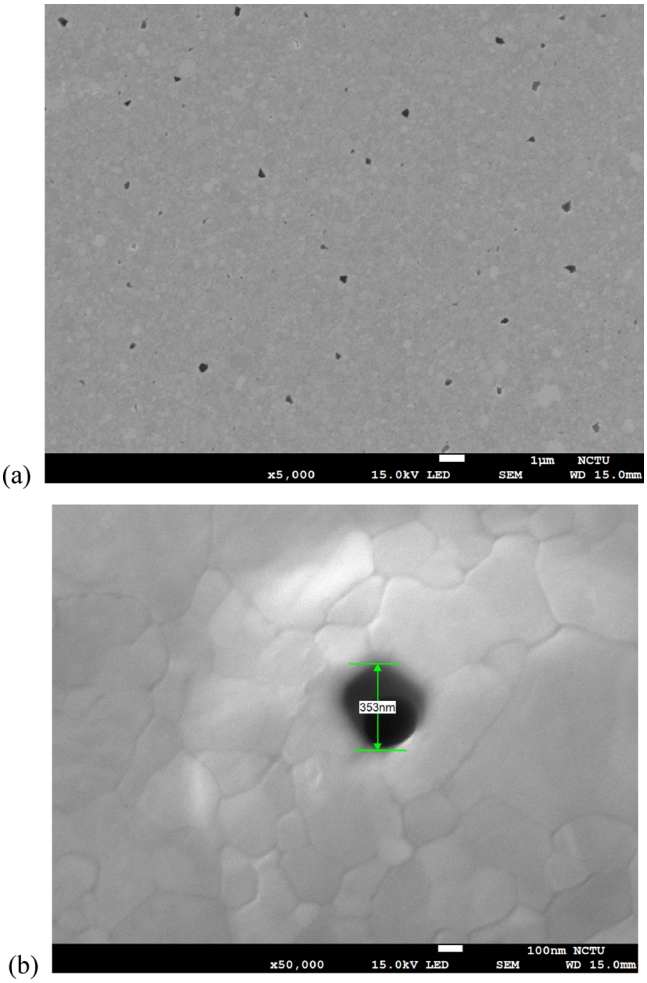

Figure 4. FE-SEM images of the Au film treated by the conventional thermal annealing at 400 °C for 1 h. (a) Several pinholes were induced during the thermal annealing. (b) Typical pinhole with a size of 353 nm.

these internal nanovoids could be driven to move outside the film gradually. Additionally, utilizing the high thermal capacity of water, the mild heating of WILSA can avoid various defects (Figure S2 in the Supporting Information).

Measurement of Optical Constants of Au Films. The optical constants (n, k) or the relative dielectric constants (ε_1, ε_2) of the Au film before and after annealing were measured by spectroscopic ellipsometry, as shown in Figure 5a,b, where the incidence angle is 75°. The data of J&C[67] and the database of

https://doi.org/10.1021/acsomega.2c05101
ACS Omega 2022, 7, 42272−42282

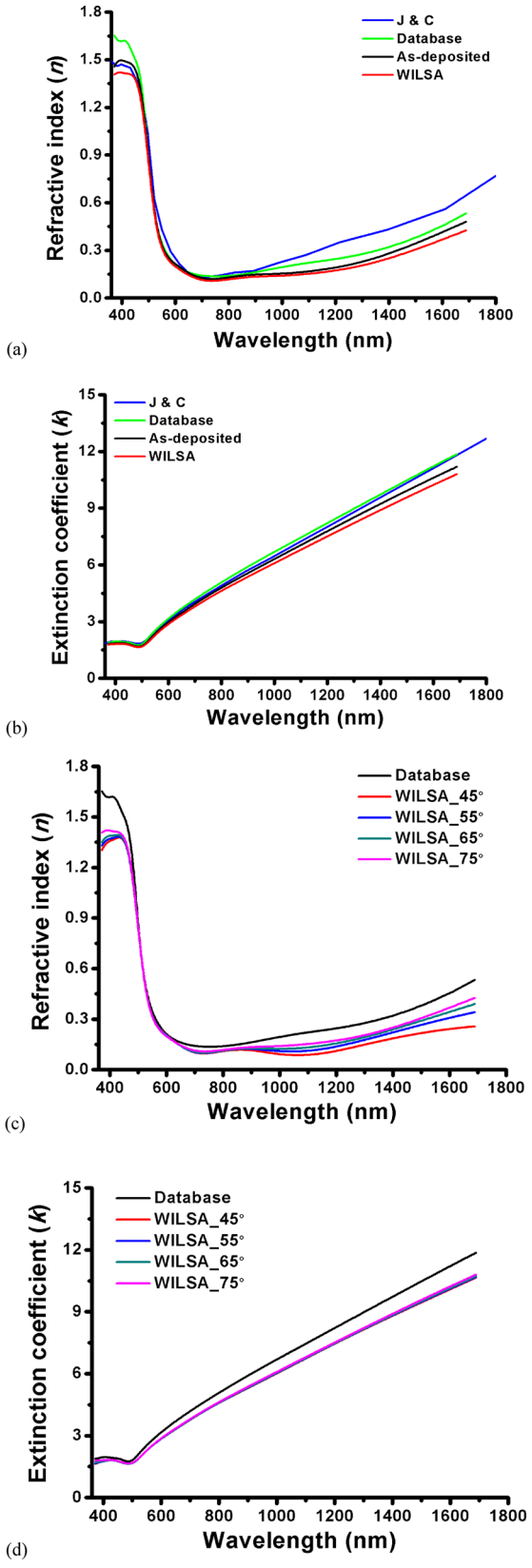

Figure 5. Optical properties of (a) n and (b) k of the Au film before and after WILSA treatment, measured at an incidence angle of 75°. The J&C data[67] (blue line) and the database of CompleteEASE are also plotted. (c) n and (d) k of the Au film before and after WILSA treatment, measured at different incidence angles (45°, 55°, 65°, and 75°).

CompleteEASE are also plotted. The K−K mode of the CompleteEASE software (J.A. Woollam Co., NE, USA) was used to maintain the consistency of the real and imaginary parts of the dielectric constants of a lossy material (Au) for the curve-fitting. Except the optical constants of the Au film, the refractive index of glass and the thicknesses of the Au film were also unknown for the inverse calculation. In addition, the effect of the adhesion layer of Ti was also assumed to be unknown for the curve-fitting; the optical properties of Ti in the database (CompleteEASE) were used. Figure 5b indicates that the extinction coefficient of the WILSA-treated Au film is significantly reduced, compared to that of an unannealed film. The reason, we think, is that the grain growth induced by the WILSA process decreases the area ratio of the amorphous or nanograin in the Au film, as shown in Figure 2a,b. As a result, the energy loss of free electrons' scattering at the grain boundaries is reduced to decrease the attenuation of plasmons, which is an interaction of photons with electrons. The reduction on the extinction coefficient of the WILSA-treated Au film is particularly significant in the NIR regime. The estimated thicknesses of Au films before and after annealing are 151 and 152.4 nm, respectively, calculated by the CompleteEASE software. These values are in agreement with the nominal thickness of 150 nm. For the refractive index n (Figure 5a), the value of the annealed film is lower than that of the unannealed one. We also measured the optical constants of the Au film at the other incidence angles (45°, 55°, and 65°), as shown in Figures 5c,d and S3 (Supporting Information). We found that these extinction coefficients k measured by different incidence angles (45°, 55°, 65°, and 75°) are almost the same. However, for a smaller incidence angle (e.g., 45°), the effect of the adhesion layer of Ti and the substrate becomes severer. Therefore, the measured refractive index n of the Au film is not accurate at a small incidence angle, particularly for a thinner Au film. The corresponding dielectric constants are also shown in Figure S4 (Supporting Information); $\varepsilon_1 + j\varepsilon_2 = n^2 - k^2 + j2nk$. Note that the optical constants of Au sensitively depend on the conditions of WILSA, such as the laser power, fluence, exposure time, and scanning step.

Optical Density. Moreover, we used a homemade spectroscopic microscope to measure the transmission of a normal-incident light through a glass coated with an Au film, as shown in Figure 1a. The ODs of the Au film obtained from the transmission spectrum were measured by transmittance spectroscopy.[2,66] Figure 6 shows the measured ODs of the 150 nm Au film before and after the WILSA treatment. We found that the OD of the WILSA-treated Au film is significantly reduced. In addition, the theoretical attenuation curves of $2\log_{10}(e)\frac{2\pi kh}{\lambda}$ are also plotted with dashed lines in Figure 6. Here, λ is the wavelength of incident light, h the thickness of Au film, and k the extinction coefficient of Au. We can simplify this problem by using an 1D layered IMI model (glass/Au film/air) to analyze the transmission of a normal-incident plane wave in terms of the optical constants of the Au film before and after the WILSA process (Figure 5). According to the Beer−Lambert law, the OD of the Au film on a glass is defined as $\mathrm{OD} = -\log_{10}\left(\frac{I}{I_0}\right)$, where I_0 is the intensity of the incident light and I is the intensity of the transmission light. In general, for a thicker Au film, the multiple reflections inside the Au film can be neglected. Consequently, the intensity of the transmission light can be approximately expressed as

https://doi.org/10.1021/acsomega.2c05101
ACS Omega 2022, 7, 42272−42282

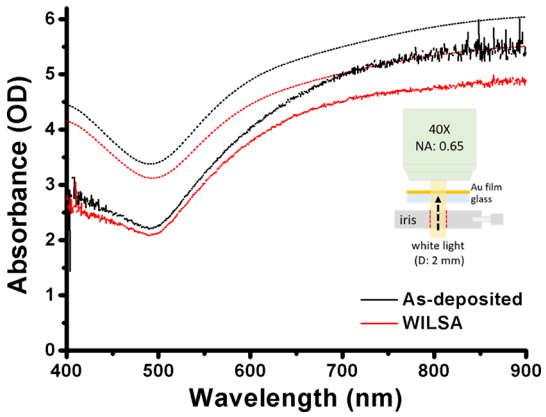

Figure 6. OD spectra of the Au film before and after WILSA treatment were obtained by the measurement of the transmission light collected by an objective lens (40×, NA: 0.65) with a 2 mm optical iris diaphragm for the light from a halogen lamp.

$$I \cong T_1 T_2 e^{-2\alpha h} I_0 \tag{1}$$

where

$$\alpha = \frac{2\pi}{\lambda}\mathrm{Im}(\sqrt{\varepsilon_1 + i\varepsilon_2}) = \frac{2\pi k}{\lambda} \tag{2}$$

Here, T_1 and T_2 are the transmission coefficients at the interfaces of glass/Au and Au/air, respectively. Hence, the theoretical OD can be approximately expressed by

$$\mathrm{OD} \approx -[\log_{10}(T_1) + \log_{10}(T_2)] + 2\log_{10}(e)\alpha h \tag{3}$$

The last term in eq 3 illustrates that the OD of the Au film depends on the thickness and the extinction coefficient.[2,66] We also used the transfer-matrix method to calculate the transmittance coefficient of a normal-incident light through an IMI layered structure (glass−Au−air) with an Au film before and after the WILSA treatment, as shown in Figure S5 (Supporting Information), where the reflections of light at the interfaces of Au/glass and Au/air were also taken into account. Figure S5 shows that the transmission coefficients of T_1 and T_2 are almost the same for the Au film before and after annealing. We can conclude that the major contribution to the decrease of OD of the Au film before and after annealing is made by the reduction of the extinction coefficient. Comparing the difference of the measured ODs with the difference of the theoretical attenuation curves, as shown in Figure 6, we can find that they are nearly consistent with each other, particularly in the NIR regime. There is a discrepancy between the measured ODs and the theoretical attenuation curves. This could be because our measurement system has an objective lens of a higher NA (0.65), whereas the theoretical curve is based on a 1D model for a plane wave transmission.

Applications of the Biosensor. In the following, two performances of an IMI layered structure with a WILSA-treated Au film are theoretically studied; one is the propagation length of a LRSPP and the other is the sensitivity on the detection of the red-shift of SPR dip for measuring the change of medium's refractive index. We used the optical constants of the unannealed and the WILSA-treated Au films, as shown in Figure 5, for the following simulations and analysis.

LRSPP. An application of the IMI layered structure for sensing is to use the attenuation of LRSPP for the detection of the amount of a specific analyte attached on the surface of the Au film quantitatively.[4] For this purpose, the propagation length of LRSPP is a crucial factor for this application. If the common time factor is $\exp(-j\omega t)$, the transcendental equation of LRSPP in the IMI three-layer structure is expressed as

$$\left(\frac{\varepsilon_2}{\varepsilon_1}\sqrt{\frac{k_1^2 - k_x^2}{k_2^2 - k_x^2}} + 1\right)\left(\frac{\varepsilon_2}{\varepsilon_3}\sqrt{\frac{k_3^2 - k_x^2}{k_2^2 - k_x^2}} + 1\right) - \left(\frac{\varepsilon_2}{\varepsilon_1}\sqrt{\frac{k_1^2 - k_x^2}{k_2^2 - k_x^2}} - 1\right)\left(\frac{\varepsilon_2}{\varepsilon_3}\sqrt{\frac{k_3^2 - k_x^2}{k_2^2 - k_x^2}} - 1\right) \exp(j2\sqrt{k_2^2 - k_x^2}h) = 0 \tag{4}$$

where h is the thickness of the metal film, k_n is ω/c_n, ε_n is the relative dielectric constant of the nth medium, and c_n is the light speed (n = 1, 2, and 3). Here, the subscript n (1, 2, 3) represents the medium; (1) the lower half-space insulator (glass), (2) metal film (Au), and (3) the upper half-space insulator (water). The unknown k_x of eq 4 is a complex wavenumber along the horizontal direction. By solving the transcendental equation numerically to find the complex roots of k_x, we can obtain the propagation length of LRSPP along an IMI layered structure of glass−Au−water; $(2Im(k_x))^{-1}$. Note that the complex roots correspond to not only the LRSPP but also the short-range SPP. Therefore, we need to reconfirm after the solving. We theoretically analyzed the dispersion relation of LRSPP along an IMI layered structure of glass−Au−water by solving a transcendental equation, where the refractive index of SiO_2 glass is 1.45. Figure 7 shows the real part of the wavenumber and the propagation length of LRSPP for three kinds of 70 nm Au films (J&C data, before and after annealing).[67] These results indicate that the propagation length of the WILSA-treated Au film is significantly larger than those of the other two, particularly in the NIR region. For example, at a typical wavelength of λ = 1550 nm the propagation length of the annealed Au film is 163 μm, whereas that of the unannealed film is 156 μm. This demonstrates that the performance of LPSPP of the IMI structure with an WILSA-treated Au film is improved, compared to that of an unannealed film.

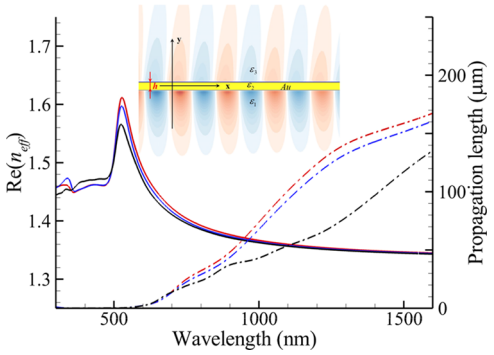

Figure 7. $Re(n_{eff})$ (solid lines) and propagation length (dashed lines) of LRSPP of IMI with 70 nm Au film versus wavelength. The J&C data[67] are also plotted (black). Red: WILSA-treated film. Blue: unannealed film.

Sensitivity of the SPR Total Internal Reflection Spectrum. The other application of an IMI structure is to use the Kretschmann−Raether type configuration for the

https://doi.org/10.1021/acsomega.2c05101
ACS Omega 2022, 7, 42272−42282

detection of the change of the medium's refractive index.[33,34] We assume that the light source is broadband with a fixed incident angle. Because of the SPR dip of the total internal reflection spectrum sensitively depending on the refractive index of the surrounding medium, we can detect the change of the refractive index quantitatively by measuring the shift of the SPR dip. The red-shift of the SPR dip increases as the refractive index of aqueous solution increases. Because the change of medium's refractive index in the near field of Au film is relevant to the concentration of a specific analyte, we can estimate the concentration quantitatively from the red-shift of the SPR dip according to a calibration line. In principle, the SPR dip of the total internal reflection spectrum of an IMI sensor (BK7−Au−water) occurs at a condition for an oblique incidence of plane wave, for example, $\theta = 68°$. The refractive index of BK7 glass is 1.5. The corresponding wavelength of the SPR dip λ_p satisfies the condition

$$n_g \sin(\theta) = Re\left(\sqrt{\frac{\varepsilon_m n_l^2}{\varepsilon_m + n_l^2}}\right) \quad (5)$$

where n_g and n_l are the refractive indexes of the glass and the solution, respectively. The relative dielectric constant of metal, $\varepsilon_m = \varepsilon_1 + j\varepsilon_2$, is a function of wavelength. Because the sensitivity and the figure of merit of this method depend on the optical quality of the Au film, an annealing process is usually recommended for the post process after Au film deposition to improve the sensitivity. Furthermore, we study the performance of the IMI structure with an unannealed or annealed 50 nm Au film theoretically by using the transfer-matrix method, where the optical constants of Figure 5 are used. Figure 8

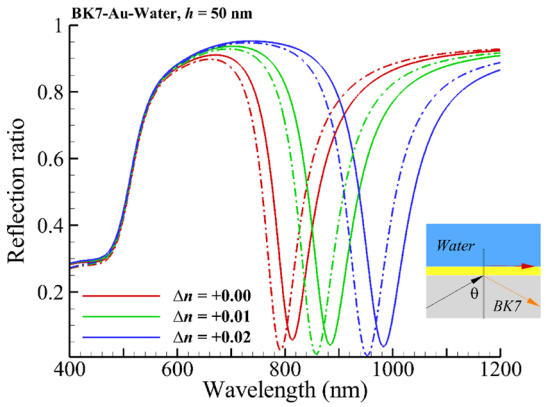

Figure 8. SPR total internal reflection spectra of the IMI structure with an unannealed or WILSA-treated Au film of 50 nm, where $\theta = 68°$. $\Delta n_l = 0.0$ (red), 0.01 (green), and 0.02 (blue) correspond to n_l of 1.33, 1.34, and 1.35, respectively. Solid lines: WILSA-treated. Dashed lines: unannealed.

shows the total internal reflection spectra of the IMI structure with unannealed and WILSA-treated Au films for an upper medium with refractive index n_l of 1.33, 1.34, and 1.35, respectively, where $\theta = 68°$. According to the wavelength shifts of SPR dips in these curves, the sensitivity, $\Delta\lambda_p/\Delta n_l$, of an annealed Au film is 8450 nm/RIU, whereas that of an unannealed film is 8050 nm/RIU. In contrast, the sensitivity of J&C data[67] is 7600 nm/RIU. The results calculated by eq 5, shown in Figure S6 (Supporting Information), are in agreement with those by the transfer-matrix method. The detailed analysis is shown in the Supporting Information. These results indicate that the sensitivity of the IMI sensor with an annealed Au film is profoundly improved, compared to the unannealed film.

In summary, the optical performances of the IMI structure in terms of the optical constants of the WILSA-treated Au film are significantly improved for the applications of biosensors, according to our analysis. The main factor in improving the optical performances is the reduction of the extinction coefficient of the Au film caused by WILSA to promote the grain growth, as indicated in Figure 5b. Note that the optimal heating conditions (laser, power, heating time, and scanning step) of the WILSA method should be properly chosen to improve the performance of the Au film with a specific thickness for realistic applications of biosensors or waveguides.

CONCLUSIONS

The improved optical properties of a WILSA-treated polycrystalline Au film were studied. Because of the grain growth caused by the laser annealing, the density of grain boundaries is reduced to diminish the loss of free electrons' scattering from the grain boundaries. Therefore, the energy loss of electrons driven by the photons via the plasmon effect is reduced. In comparison with the unannealed film, the extinction coefficient of optical constants of the WILSA-treated Au film, characterized by spectroscopic ellipsometry in the visible to NIR regime, is significantly reduced. We also found that the OD of the annealed Au film deposited on a glass is decreased. In terms of the optical constants of the Au film before and after annealing, the estimated ODs by using the theoretical analysis are consistent with the measured ODs by transmittance spectroscopy. The significant reduction of OD is mainly correlated with the reduced extinction coefficient (the imaginary part of the refractive index) of an annealed Au film. An advantage of the WILSA method is that the local overheating is avoided by using the high heat capacity of water to carry away the excess heat in the Au film. Another advantage of this method is that the point-scanning laser heating provides a temperature gradient to facilitate the local migration of grain boundaries. Consequently, the integrity of the treated thin film is kept intact without producing pinholes. The material characterization using XRD, FE-SEM, and EBSD shows the improved crystallinity with a more uniform crystallographic orientation of (111) and the grain growth of the WILSA-treated Au film.

Furthermore, through the theoretical analysis, the propagation length of a LRSPP along an IMI structure with the WILSA-treated Au film is significantly increased, compared to that with an unannealed film, particularly in the NIR regime. In addition, the sensitivity of an IMI sensor with an annealed film for the measurement of the change of the medium's refractive index is profoundly improved. Our WILSA method provides a new postprocess to the quality improvement of a deposited polycrystalline Au film for the applications of related biosensors by raising their sensitivity and figure of merit. It is worth mentioning that the optimal heating conditions (laser wavelength, fluence, exposure time, and scanning step) need to be adjusted for different thicknesses. This technology might be applied to improve the intrinsic optical properties of the other metal, for example, Cu, Ag, and Al, films deposited on a substrate for a variety of applications for biosensors and optoelectronic devices. In addition, the selective area annealing is a uniqueness of the WILSA method for specific nanostructures.

https://doi.org/10.1021/acsomega.2c05101
ACS Omega 2022, 7, 42272−42282

■ ASSOCIATED CONTENT

Supporting Information

The Supporting Information is available free of charge at https://pubs.acs.org/doi/10.1021/acsomega.2c05101.

Bright-field images of Au films as deposited, after the WILSA treatment, and after the conventional thermal annealing; FE-SEM images of Au film treated by the conventional thermal annealing at 400 °C for 1 h; optical constants (n, k) of the Au film before and after WILSA treatment, measured by different incident angles (45° and 75°); relative dielectric constants (ε_1, ε_2) of the Au film after the WILSA treatment, measured by different incidence angles (45°, 55°, 65°, and 75°); ODs of an Au film deposited on a glass before and after the WILSA treatment, calculated by the transfer-matrix method; configuration of a LRSPP propagating along the horizontal direction (x-axis) of an IMI three-layer structure; the wavelengths of the SPR dip calculated by eq 4 for J&C data,[67] and the unannealed Au film and WILSA-treated Au film, respectively (PDF)

■ AUTHOR INFORMATION

Corresponding Author

Jiunn-Woei Liaw − *Department of Mechanical Engineering, Chang Gung University, Taoyuan 333323, Taiwan; Department of Mechanical Engineering, Ming Chi University of Technology, New Taipei 243303, Taiwan; Proton and Radiation Therapy Center, Linkou Chang Gung Memorial Hospital, Taoyuan 333011, Taiwan;* orcid.org/0000-0003-0179-5274; Email: markliaw@mail.cgu.edu.tw

Authors

Shang-Yang Yu − *Department of Mechanical Engineering, Chang Gung University, Taoyuan 333323, Taiwan;* orcid.org/0000-0002-0382-8423

Min-Hsiung Shih − *Research Center for Applied Sciences, Academia Sinica, Taipei 115201, Taiwan;* orcid.org/0000-0002-5627-7098

Yun-Cheng Ku − *Institute of Applied Mechanics, National Taiwan University, Taipei 106, Taiwan*

Yi-Han Kuo − *Department of Mechanical Engineering, Chang Gung University, Taoyuan 333323, Taiwan*

Complete contact information is available at: https://pubs.acs.org/10.1021/acsomega.2c05101

Author Contributions

J.W.L. proposed the initial idea and designed the research together with M.H.S. S.Y.Y. performed the experiments and measurements. M.H.S. prepared the specimens and provided suggestions. Y.C.K. simulated the models. Y.H.K. designed and fabricated the fluidic chamber. J.W.L. and S.Y.Y. wrote the manuscript through contributions of all authors. All authors have given approval to the final version of the manuscript.

Notes

The authors declare no competing financial interest.

■ ACKNOWLEDGMENTS

The research was supported by Ministry of Science and Technology, Taiwan (MOST 110-2221-E-182-039-MY3 and 110-2221-E-182-038-MY2) and Chang Gung Memorial Hospital (CIRPD2I0023). The authors thank the Microscopy Center at Chang Gung University and the Research Center for Intelligent Medical Devices at Ming Chi University of Technology for technical assistance. The authors thank Prof. Li-Chun Chang, Department of Materials Engineering in Ming Chi University of Technology, for providing a thermal-annealing furnace (SJ-OV400, Lindberg/Blue M). Authors also thank Prof. Kuo-Yung Hung, Department of Mechanical Engineering in Ming Chi University of Technology, Prof. Jong-Hong Lu, Department of Materials Engineering in Ming Chi University of Technology, and Prof. Mao-Kuen Kuo, Institute of Applied Mechanics in National Taiwan University, for providing useful advices on various technical and theoretical issues.

■ REFERENCES

(1) McPeak, K. M.; Jayanti, S. V.; Kress, S. J. P.; Meyer, S.; Iotti, S.; Rossinelli, A.; Norris, D. J. Plasmonic films can easily be better: rules and recipes. *ACS Photonics* **2015**, *2*, 326−333.

(2) Schaub, A.; Slepička, P.; Kašpárková, I.; Malinský, P.; Macková, A.; Švorčík, V. Gold nanolayer and nanocluster coatings induced by heat treatment and evaporation technique. *Nanoscale Res. Lett.* **2013**, *8*, 249.

(3) Bosman, M.; Zhang, L.; Duan, H.; Tan, S. F.; Nijhuis, C. A.; Qiu, C.-W.; Yang, J. K. W. Encapsulated annealing: enhancing the plasmon quality factor in lithographically−defined nanostructures. *Sci. Rep.* **2014**, *4*, 5537.

(4) Chen, Y.; Wang, J.; Chen, X.; Yan, M.; Qiu, M. Plasmonic analog of microstrip transmission line and effect of thermal annealing on its propagation loss. *Opt. Express* **2013**, *21*, 1639−1644.

(5) Chou, B.-T.; Lin, S.-D.; Huang, B.-H.; Lu, T.-C. Single-crystalline silver film grown on Si (100) substrate by using electron-gun evaporation and thermal treatment. *J. Vac. Sci. Technol., B* **2014**, *32*, No. 031209.

(6) Zhang, F.; Proust, J.; Gérard, D.; Plain, J.; Martin, J. Reduction of plasmon damping in aluminum nanoparticles with rapid thermal annealing. *J. Phys. Chem. C* **2017**, *121*, 7429−7434.

(7) Syed, M.; Glaser, C.; Hynes, C.; Syed, M. Thermal annealing of gold thin film on the structure and surface morphology using RF magnetron sputtering. *J. Mater. Sci. Eng. B* **2018**, *8*, 66−76.

(8) Shen, P. T.; Sivan, Y.; Lin, C.-W.; Liu, H.-L.; Chang, C.-W.; Chu, S.-W. Temperature and roughness dependent permittivity of annealed/unannealed gold films. *Opt. Express* **2016**, *24*, 19254−19263.

(9) Švorčík, V.; Siegel, J.; Šutta, P.; Mistrík, J.; Janíček, P.; Worsch, P.; Kolská, Z. Annealing of gold nanostructures sputtered on glass substrate. *Appl. Phys. A: Mater. Sci. Process.* **2011**, *102*, 605−610.

(10) Zhang, C.; Li, J.; Belianinov, A.; Ma, Z.; Renshaw, C. K.; Gelfand, R. M. Nanoaperture fabrication in ultra-smooth single-grain gold films with helium ion beam lithography. *Nanotechnology* **2020**, *31*, 465302.

(11) Gall, D. Electron mean free path in elemental metals. *J. Appl. Phys.* **2016**, *119*, No. 085101.

(12) Schlesinger, Z.; Sievers, A. J. IR Surface plasmon attenuation coefficients for Ag and Au films. *Solid State Commun.* **1982**, *43*, 671−673.

(13) Sambles, J. R. Grain-boundary scattering and surface plasmon attenuation in noble metal films. *Solid State Commun.* **1984**, *49*, 343−345.

(14) Jiang, Y.; Pillai, S.; Green, M. A. Grain boundary effects on the optical constants and Drude relaxation times of silver films. *J. Appl. Phys.* **2016**, *120*, 233109.

(15) Zhang, S.; Pei, Y.; Liu, L. Dielectric function of polycrystalline gold films: effects of grain boundary and temperature. *J. Appl. Phys.* **2018**, *124*, 165301.

(16) Chen, K.-P.; Drachev, V. P.; Borneman, J. D.; Kildishev, A. V.; Shalaev, V. M. Drude relaxation rate in grained gold nanoantennas. *Nano Lett.* **2010**, *10*, 916−922.

(17) Yakubovsky, D. I.; Arsenin, A. V.; Stebunov, Y. V.; Fedyanin, D. Y.; Volkov, V. S. Optical constants and structural properties of thin gold films. *Opt. Express* **2017**, *25*, 25574−25587.
(18) Hilfiker, J. N.; Singh, N.; Tiwald, T.; Convey, D.; Smith, S. M.; Baker, J. H.; Tompkins, H. G. Survey of methods to characterize thin absorbing films with spectroscopic ellipsometry. *Thin Solid Films* **2008**, *516*, 7979−7989.
(19) Secondo, R.; Fomra, D.; Izyumskaya, N.; Avrutin, V.; Hilfiker, J. N.; Martin, A.; Özgur, U.; Kinsey, N. Reliable modeling of ultrathin alternative plasmonic materials using spectroscopic ellipsometry. *Opt. Mater. Express* **2019**, *9*, 760−770.
(20) Olmon, R. L.; Slovick, B.; Johnson, T. W.; Shelton, D.; Oh, S.-H.; Boreman, G. D.; Raschke, M. B. Optical dielectric function of gold. *Phys. Rev. B: Condens. Matter Mater. Phys.* **2012**, *86*, No. 235147.
(21) Mori, T.; Fujii, M.; Tominari, Y.; Otomo, A.; Yamaguchi, K. Optical properties of low-loss Ag films and nanostructures on transparent substrates. *ACS Appl. Mater. Interfaces* **2018**, *10*, 8333−8340.
(22) Reddy, H.; Guler, U.; Kildishev, A. V.; Boltasseva, A.; Shalaev, V. M. Temperature-dependent optical properties of gold thin films. *Opt. Mater. Express* **2016**, *6*, 2776−2802.
(23) Pham, A. H.; Fukunaga, N.; Yeh, W.; Morito, S.; Ohba, T. Rapid annealing of Au thin films by micron chevron-shaped laser beam scanning toward growth of single-grain crystal. *Jpn. J. Appl. Phys.* **2021**, *60*, SBBK06.
(24) Heinig, M. F.; Chatterjee, D.; van Helvoort, A. T. J.; Wagner, J. B.; Kadkhodazadeh, S.; Ånes, H. W.; Niessen, F.; da Silva Fanta, A. B. High resolution crystal orientation mapping of ultrathin films in SEM and TEM. *Mater. Charact.* **2022**, *189*, No. 111931.
(25) Chang, P.; Liu, K.; Jiang, J.; Zhang, Z.; Ma, J.; Zhang, J.; Li, X.; Liu, T. Performance enhancement of the surface plasmon resonance sensor through the annealing process. *IEEE Access* **2020**, *8*, 33990−33997.
(26) Zhang, J.; Irannejad, M.; Yavuz, M.; Cui, B. Gold nanohole array with sub-1 nm roughness by annealing for sensitivity enhancement of extraordinary optical transmission biosensor. *Nanoscale Res. Lett.* **2015**, *10*, 238.
(27) Chiang, H.-P.; Lin, J.-L.; Chen, Z.-W. High sensitivity surface plasmon resonance sensor based on phase interrogation at optimal incident wavelengths. *Appl. Phys. Lett.* **2006**, *88*, 141105.
(28) Hiramatsu, N.; Kusa, F.; Imasaka, K.; Morichika, I.; Takegami, A.; Ashihara, S. Propagation length of mid-infrared surface plasmon polaritons on gold: impact of morphology change by thermal annealing. *J. Appl. Phys.* **2016**, *120*, 173103.
(29) Burke, J. J.; Stegeman, G. I.; Tamir, T. Surface-polariton-like waves guided by thin, lossy metal films. *Phys. Rev. B: Condens. Matter Mater. Phys.* **1986**, *33*, 5186−5201.
(30) Krupin, O.; Asiri, H.; Wang, C.; Tait, R. N.; Berini, P. Biosensing using straight long-range surface plasmon waveguides. *Opt. Express* **2013**, *21*, 698−709.
(31) Wong, W. R.; Krupin, O.; Adikan, F. R. M.; Berini, P. Optimization of long-range surface plasmon waveguides for attenuation-based biosensing. *J. Lightwave Technol.* **2015**, *33*, 3234−3242.
(32) Min, Q.; Chen, C.; Berini, P.; Gordon, R. Long range surface plasmons on asymmetric suspended thin film structures for biosensing applications. *Opt. Express* **2010**, *18*, 19009−19019.
(33) Piliarik, M.; Homola, J. Surface plasmon resonance (SPR) sensors: approaching their limits? *Opt. Express* **2009**, *17*, 16505−16517.
(34) Gryga, M.; Dalibor Ciprian, D.; Hlubina, P. Bloch surface wave resonance based sensors as an alternative to surface plasmon resonance sensors. *Sensors* **2020**, *20*, 5119.
(35) Chen, L.; Khristosov, M. K.; Saguy, C.; Katsman, A.; Pokroy, B. Association between gold grain orientation and its periodic steps formed at the gold/substrate interface. *J. Phys. Chem. C* **2018**, *122*, 11364−11370.
(36) Abbott, W. M.; Corbett, S.; Cunningham, G.; Petford-Long, A.; Zhang, S.; Donegan, J. F.; McCloskey, D. Solid state dewetting of thin plasmonic films under focused cw-laser irradiation. *Acta Mater.* **2018**, *145*, 210−219.
(37) Magnozzi, M.; Bisioa, F.; Canepa, M. Solid-state dewetting of thin Au films studied with real-time, in situ spectroscopic ellipsometry. *Appl. Surf. Sci.* **2017**, *421*, 651−655.
(38) Abbott, W. M.; Murray, W. M.; Zhong, C.; Smith, C.; McGuinness, C.; Rezvani, E.; Downing, C.; Daly, D.; Petford-Long, A. K.; Bello, F.; McCloskey, D.; Donegan, J. F. Less is more: improved thermal stability and plasmonic response in Au films via the use of subnanometer Ti adhesion layers. *ACS Appl. Mater. Interfaces* **2019**, *11*, 7607−7614.
(39) Palli, S.; Dey, S. R. Thermal stability of pulse electroplated gold films: SEM-EBSD studies. *Adv. Mater. Sci.* **2017**, *2*, No. 1000118.
(40) Karim, S.; Toimil-Molares, M. E.; Balogh, A. G.; Ensinger, W.; Cornelius, T. W.; Khan, E. U.; Neumann, R. Morphological evolution of Au nanowires controlled by Rayleigh instability. *Nanotechnology* **2006**, *17*, 5954−5959.
(41) Kim, J.; Lin, C.-Y.; Xing, W.; Mecartney, M. L.; Potma, E. O.; Penner, R. M. Laser annealing of nanocrystalline gold nanowires. *ACS Appl. Mater. Interfaces* **2013**, *5*, 6808−6814.
(42) Sharif, A.; Farid, N.; Vijayaraghavan, R. K.; McNally, P. J.; O'Connor, G. M. Femtosecond laser assisted crystallization of gold thin film. *Nanomaterials* **2021**, *11*, 1186.
(43) Xu, M.; Peng, C.; Yuan, Y.; Li, X.; Zhang, J. Enhancing the performance of solution-processed thin-film transistors via laser scanning annealing. *ACS Appl. Electron. Mater.* **2020**, *2*, 2970−2975.
(44) Chen, X.; Chen, Y.; Dai, J.; Yan, M.; Zhao, D.; Li, Q.; Qiu, M. Ordered Au nanocrystals on a substrate formed by light-induced rapid annealing. *Nanoscale* **2014**, *6*, 1756−1762.
(45) Zdeněk, V.; Milan, H.; Jiří, M. 3D model of laser treatment by a moving heat source with general distribution of energy in the beam. *Appl. Opt.* **2016**, *55*, D140−D150.
(46) Sharif, A.; Farid, N.; Vijayaraghavan, R. K.; McNally, P. J.; O'Connor, G. M. Femtosecond laser assisted crystallization of gold thin films. *Nanomaterials* **2021**, *11*, 1186.
(47) Tan, Y.; Maniatty, A. M.; Zheng, C.; Wen, J. T. Monte Carlo grain growth modeling with local temperature gradient. *Modell. Simul. Mater. Sci. Eng.* **2017**, *25*, No. 065003.
(48) Zollner, D. Impact of a strong temperature gradient on grain growth in films. *Modell. Simul. Mater. Sci. Eng.* **2022**, *30*, No. 025010.
(49) Gusak, A. M.; Chen, K.-J.; Tu, K. N.; Chen, C. Modeling of abnormal grain growth in (111) oriented and nanotwinned copper. *Sci. Rep.* **2021**, *11*, 20449.
(50) Kusar, P.; Gruber, C.; Hohenau, A.; Krenn, J. R. Measurement and reduction of damping in plasmonic nanowires. *Nano Lett.* **2012**, *12*, 661−665.
(51) Huang, J.-S.; Callegari, V.; Geisler, P.; Bruning, C.; Kern, J.; Prangsma, J. C.; Wu, X.; Feichtner, T.; Ziegler, J.; Weinmann, P.; Kamp, M.; Forchel, A.; Biagioni, P.; Sennhauser, U.; Hecht, B. Atomically flat single-crystalline gold nanostructures for plasmonic nanocircuitry. *Nat. Commun.* **2010**, *1*, 150.
(52) Prämassing, M.; Liebtrau, M.; Schill, H. J.; Irsen, S.; Linden, S. Interferometric near-field characterization of plasmonic slot waveguides in single- and poly-crystalline gold films. *Opt. Express* **2020**, *28*, 12998−13005.
(53) Méjard, R.; Verdy, A.; Demichel, O.; Petit, M.; Markey, L.; Herbst, F.; Chassagnon, R.; Colas-des-Francs, G.; Cluzel, B.; Bouhelier, A. Advanced engineering of single-crystal gold nanoantennas. *Opt. Mater. Express* **2017**, *7*, 1157−1168.
(54) Liu, H.-W.; Lin, F.-C.; Lin, S.-W.; Wu, J.-Y.; Chou, B.-T.; Lai, K.-J.; Lin, S.-D.; Huang, J.-S. Single-crystalline aluminum nanostructures on a semiconducting GaAs substrate for ultraviolet to near-infrared plasmonics. *ACS Nano* **2015**, *9*, 3875−3886.
(55) Cheng, F.; Su, P.-H.; Choi, J.; Gwo, S.; Li, X.; Shih, C.-K. Epitaxial growth of atomically smooth aluminum on silicon and its intrinsic optical properties. *ACS Nano* **2016**, *10*, 9852−9860.
(56) Chou, Y.-H.; Wu, Y.-M.; Hong, K.-B.; Chou, B.-T.; Shih, J.-H.; Chung, Y.-C.; Chen, P.-Y.; Lin, T.-R.; Lin, C.-C.; Lin, S.-D.; Lu, T.-C.

https://doi.org/10.1021/acsomega.2c05101
ACS Omega 2022, 7, 42272−42282

High-operation-temperature plasmonic nanolasers on single-crystalline aluminum. *Nano Lett.* **2016**, *16*, 3179−3186.
(57) Cheng, F.; Lee, C.-J.; Choi, J.; Wang, C.-Y.; Zhang, Q.; Zhang, H.; Gwo, S.; Chang, W.-H.; Li, X.; Shih, C.-K. Epitaxial growth of optically thick, single crystalline silver films for plasmonics. *ACS Appl. Mater. Interfaces* **2019**, *11*, 3189−3195.
(58) Choi, J.; Cheng, F.; Cleary, J. W.; Sun, L.; Dass, C. K.; Hendrickson, J. R.; Wang, C.-Y.; Gwo, S.; Shih, C.-K.; Li, X. Optical dielectric constants of single crystalline silver films in the long wavelength range. *Opt. Mater. Express* **2020**, *10*, 693−703.
(59) Fedotov, V. A.; Uchino, T.; Ou, J. Y. Low-loss plasmonic metamaterial based on epitaxial gold monocrystal film. *Opt. Express* **2012**, *20*, 9545−9550.
(60) Chew, S. H.; Gliserin, A.; Choi, S.; Geng, X.-T.; Kim, S.; Hwang, W.; Baek, K.; Anh, N. D.; Kim, Y.-J.; Song, Y. M.; et al. Large-area grain-boundary-free copper films for plasmonics. *Appl. Surf. Sci.* **2020**, *521*, No. 146377.
(61) Kumar, S.; Lu, Y.-W.; Huck, A.; Andersen, U. L. Propagation of plasmons in designed single crystalline silver nanostructures. *Opt. Express* **2012**, *20*, 24614−24622.
(62) Park, J. H.; Ambwani, P.; Manno, M.; Lindquist, N. C.; Nagpal, P.; Oh, S.-H.; Leighton, C.; Norris, D. J. Single-crystalline silver films for plasmonics. *Adv. Mater.* **2012**, *24*, 3988−3992.
(63) Mori, T.; Mori, T.; Tanaka, Y.; Suzaki, Y.; Yamaguchi, K. Fabrication of single-crystalline plasmonic nanostructures on transparent and flexible amorphous substrates. *Sci. Rep.* **2017**, *7*, 42859.
(64) Grayli, S. V.; Zhang, X.; MacNab, F. C.; Kamal, S.; Leach, G. W. Scalable, green fabrication of single-crystal noble metal films and nanostructures for low-loss nanotechnology applications. *ACS Nano* **2020**, *14*, 7581−7592.
(65) Setoura, K.; Okada, Y.; Werner, D.; Hashimoto, S. Observation of nanoscale cooling effects by substrates and the surrounding media for single gold nanoparticles under CW-Laser illumination. *ACS Nano* **2013**, *7*, 7874−7885.
(66) Joensen, P.; Irwin, J. C.; Cochran, J. F.; Curzon, A. E. Transmission method for determining the optical constants of metals. *J. Opt. Soc. Am.* **1973**, *63*, 1556−1562.
(67) Johnson, P. B.; Christy, R. W. Optical constants of the noble metals. *Phys. Rev. B: Solid State* **1972**, *6*, 4370−4379.

https://doi.org/10.1021/acsomega.2c05101
ACS Omega 2022, 7, 42272−42282